Two-dimensional graphitic carbon nitrides: Strain-tunable ferromagnetic ordering

A. Bafekry [*]
Department of physics, University of Guilan, 41335-1914 Rasht, Iran
and Department of Physics, University of Antwerp, Groenenborgerlaan 171, B-2020 Antwerp, Belgium

M. Neek-Amal [†]
Department of Physics, Shahid Rajaee Teacher Training University, 16875-163 Lavizan, Tehran, Iran

F. M. Peeters [‡]
Department of Physics, University of Antwerp, Groenenborgerlaan 171, B-2020 Antwerp, Belgium

(Received 23 October 2019; revised manuscript received 22 January 2020; accepted 18 March 2020; published 6 April 2020)

Using first-principle calculations, we systematically study strain tuning of the electronic properties of two-dimensional graphitic carbon nitride nanosheets with empirical formula C_nN_m. We found the following: (i) the ferromagnetic ordered state in the metal-free systems $(n, m) = (4,3)$, (10,9), and (14,12) remains stable in the presence of strain of about 6%. However, the system (9,7) loses its ferromagnetic ordering when increasing strain. This is due to the presence of topological defects in the (9,7) system, which eliminates the asymmetry between spin up and spin down of the p_z orbitals when strain is applied. (ii) By applying uniaxial strain, a band gap opens in systems which are initially gapless. (iii) In semiconducting systems which have an initial gap of about 1 eV, the band gap is closed with applying uniaxial strain.

DOI: 10.1103/PhysRevB.101.165407

I. INTRODUCTION

Two-dimensional (2D) materials beyond graphene, such as carbon nitride, silicene, and many others, are considered to be good candidates for the realization of the quantum spin Hall effect at nonzero temperature [1]. Among these materials, the two-dimensional graphitic carbon nitride (2DGCN) is a new class of nanomaterials that has attracted a lot of attention during the past few years [2–7]. The 2DGCN crystal with chemical formula C_nN_m is labeled by the (n, m) index, where n is the number of carbon atoms and m is the number of nitrogen atoms in the corresponding primitive cell. The 2DGCNs may have applications in both energy and environment and exhibit outstanding properties [8–11]. For instance, the system (2,1) is a candidate for filtration and adsorption of atoms [2,12], while the systems (3,1) and (3,4) are two-dimensional polyaniline and photocatalyst, respectively [12–19].

The electronic and magnetic properties of 2DGCN can be drastically different from those of graphene and other two-dimensional materials because of the presence of nitrogen atoms. It is known that although the system (4,3) is a half metal [20], the system (3,4) is a semiconductor. In a recent theoretical work, it was shown that the system (6,6) exhibits a nontrivial band gap which can be modulated to a topological insulator by hydrogen doping [21]. The successful synthesis of different 2DGCN nanosheets such as (2,1), (3,1), (3,4), (6,8), and (6,6) was shown to have interesting semiconducting characteristics which are promising for numerous applications [2,8,22,23].

Recently, Zhang and Zhao [1], using density functional theory (DFT), reported that a moderate band gap of 3.7 meV is opened in the system (14,12), which was found to be due to the intrinsic spin-orbit interaction at the Fermi level. Moreover, their calculations confirmed that (14,12) is a two-dimensional magnetic topological insulator having a Chern number equal to -1. The physical origins of the relatively strong spin-orbit coupling and stable ferromagnetic ordered state are due to the presence of $p_{x,y}$ atomic orbitals. Furthermore, using a Monte Carlo simulation and Ising model, Li *et al.* [24] found the variation of magnetization per unit cell of a g-C_4N_3-based kagome lattice with respect to temperature. It was reported that the ferromagnetic state of the g-C_4N_3-based kagome lattice is preserved above room temperature, and thus the ferromagnetism in this 2DGCN is stable and might be detected at room temperature [24].

In the present paper, we performed extensive density functional theory (DFT) calculations on 12 different (n, m) systems. In order to tune their electronic properties, we applied in-plane strain. We found that in the systems (14,12), (4,3), and (10,9), the ferromagnetic ordering is stable even for strain up to 6%, while the system (9,7) gradually loses its magnetic ordered state under strain. The systems which are initially gapless open a gap of about 50–300 meV when they are subjected to strain of about 8%.

[*]Bafekry.asad@gmail.com
[†]mehdi.neekamal@gmail.com
[‡]francois.peeters@uantwerpen.be

TABLE I. The structural, electronic, and magnetic parameters of graphene and 2DGCN nanosheets, including lattice constant a, the bond length between C-C atoms (d_{CC}), the bond length between N-C atoms (d_{NC}), the diameter of the nanopore (D_{NP}), the band gap of the systems (Δ), and the Young's modulus (Y). Electronic states are specified as metal (M), semimetal (SM), half metal (HM), ferromagnetic metal (FM), metal (M), dilute magnetic (DM) semiconductor, spin-glass semiconductor (SG-SC), semiconductor (SC), and the magnetic moment per supercell M_{tot}. The state of the systems in the presence of strain of 0% (4%) is shown in the sixth (last) column.

2DGCN	a (Å)	d_{CC} (Å)	d_{NC} (Å)	D_{NP} (Å)	Δ (eV) ($\varepsilon = 0\%$)	$M_{tot}(\mu_B)$	$\varepsilon = 4\%$	Y (TPas)
(2,1)	8.35	1.457,1.430	1.342	5.503	SC (1.75)	0	SC	
(3,1)	4.86	1.404	1.403		SC (0.4)	0	SC	1.02
(3,4)	4.74		1.323,1.445	2.728	SC (1.45)	0	SC	
(6,6)	7.11	1.503	1.343	5.447	SC (1.5)	0	SC	
(6,8)	7.14		1.414–1.455	4.773	SC (1.22)	0	SC	
(4,1)	4.775	1.445	1.443		SM	0	SC	0.5
(3,2)	8.70	1.402,1.511	1.354,1.392	4.254,5.454	M	0	M	
(9,4)	9.72	1.428,1.470	1.348,1.407	5.588	SM	0	SC	
(4,3)	4.81	1.427	1.346	2.736	HM (2.2(↑))	1	HM	0.09
(9,7)	8.05	1.414,1.488	1.385,1.444	5.472	FM	0.8	FM	0.03
(10,9)	9.86	1.418,1.502	1.370,1.385	7.300	SG-SC (1.7(↑))	1	DM-SC	0.011
(14,12)	11.77	1.435	1.365	9.301	SG-SC (2.1(↑))	2	HM	0.002

II. METHOD

We carried out first-principles total-energy and electronic structure calculations, within the Perdew-Burke-Ernzerhof variant of the generalized gradient approximation (PBE-GGA) [25] method as implemented in the OPENMX package [26]. We used norm-conserving pseudopotentials [27]. The wave functions are expanded in linear combinations of multiple pseudoatomic orbitals (LCPAOs) that one generated using a confinement scheme [26,28]. After the convergence tests, we chose different cutoff energies for 2DGCN, so that the total energies converge below 1.0 meV/atom. The geometries were fully relaxed until the force acting on each atom was less than 1 meV/Å. With these parameters, the resulting structures are found to be sufficiently relaxed in order to obtain various properties in the next steps of the calculation. The k points for sampling over the Brillouin zone (BZ) integration were generated using the Monkhorst-Pack scheme [29]. A k-mesh grid of $23 \times 23 \times 1$ was used for a primitive unit cell and scaled according to the size of the supercell. The 2DGCNs are modeled as a periodic slab with a sufficiently large vacuum layer (20 Å) in order to avoid interaction between adjacent layers.

III. ELECTRONIC STRUCTURE OF 2DCGN

First, we report on the structural and electronic properties of 12 studied 2DGCN nanosheets, which are listed in Table I. We found that the planar minimum-energy configurations of the systems (2,1), (3,1), (3,4), (6,6), and (6,8) reveal semiconducting (SC) characteristics, which is in agreement with previous reports [3,30–33] (see Fig. 1).

It is well known that the lattice symmetry of a 2D-hexagonal system (such as graphene and most of the studied 2DGCNs) has the $P6/mmm$ space group. For instance, the system (3,1) has both center and mirror symmetries with a sp^2 hybridization in the C-N bonds, similar to the atoms in graphene, while the hybridization in C-N bonds of (4,1) is sp^3, similar to the C-C bonds in diamond. For the planar systems such as (9,4) and (14,12), sixfold rotational symmetry is preserved. Some of the other systems have threefold [(9,7)] and fourfold [(3,2)] symmetry. It is also interesting to note that the system (14,12) displays characteristics of a perfect kagome lattice [1], where six equilateral triangles surround a central hexagon, and vice versa. The nonplanar system (4,1) has less symmetry as compared to (3,1) because of the absence of center symmetric.

On the other hand, by destroying the honeycomb lattice structure, the carrier mobility can be greatly reduced because of the scattering centers due to the presence of intrinsic porosity in the systems (holey 2D crystal). The latter could enhance the carrier effective mass as compared to zero mass in graphene. In an ideal case of graphene at the Dirac point, the carrier's mass for both electron and hole is zero. The effective mass for the graphene/g-(4,3) heterostructure is found to be nonzero and two orders of magnitude smaller than the electron mass [34].

On the other hand (see Fig. 2), the system (3,2) shows metallic (M) properties and the systems (9,4) and (4,1) show semimetal (SM) properties where energy bands touch each other at E_F, resulting in the appearance of one or more Dirac points. Our results are in agreement with previous calculations by Chen *et al.* [35] (see Fig. 2).

Among all of the listed 2DGCN structures in Table I, four systems (4,3), (9,7), (10,9), and (14,12) reveal ferromagnetic ordering; see Fig. 3. The lattice parameters of (4,3) are found to be 4.81 Å and the carbon-carbon bond length (d_{CC}) and carbon-nitrogen bond length (d_{NC}) were found to be 1.427 and 1.346 Å, respectively. These numbers are in good agreement with a previous report [36]. The primitive unit cell of the system (9,7) has one hexagon of carbon surrounded by three C-N pentagons [see second panel in Fig. 3(a)]. The lattice constant of this system was found to be 8.050 Å. The completely planar structure and the features of the bond lengths and bond angles imply that the chemical bonds in the system (9,7) ought to be covalent [37]. The lattice constant of the system (10,9) was found to be 9.86 Å and d_{CC} bridging building blocks is 1.502 Å, which is longer than that around

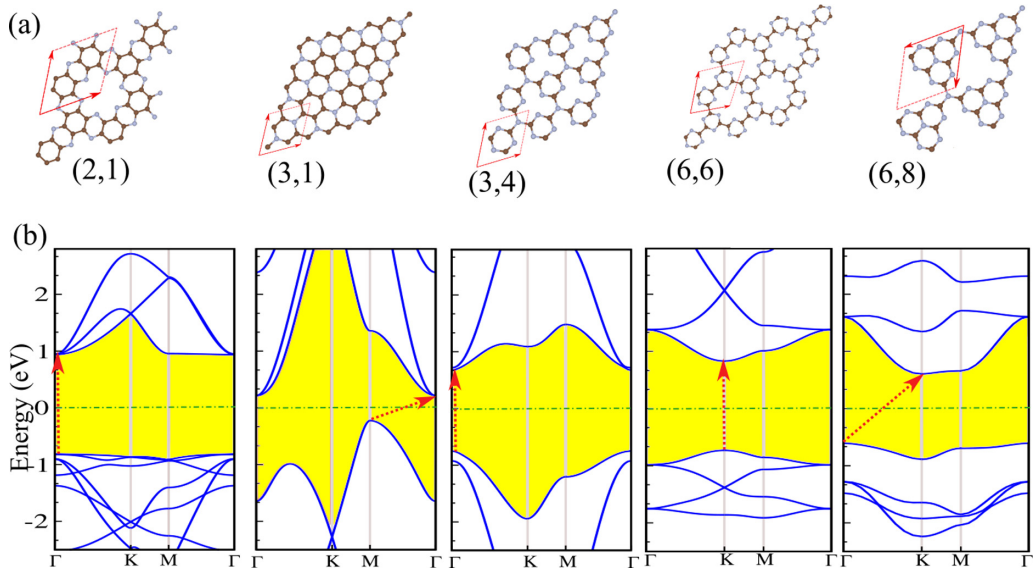

FIG. 1. (a) Geometric atomic structure of the semiconducting systems (2,1), (3,1), (3,4), (6,6), and (6,8). The primitive unit cell is denoted by a red parallelogram. (b) The corresponding electronic band structure. Here the zero of energy is set to the Fermi level. The arrows refer to the band gap.

the center of the unit cell (i.e., 1.418 Å) [38]. The system (14,12) has a lattice constant of 11.77 Å with a planar 2D structure. The corresponding d_{CC} and d_{NC} were found to be 1.435 and 1.365 Å, respectively. Our results are consistent with those reported in Ref. [38]. Note that the systems (4,1) and (4,3) have a sandwiched structure and are not flat [see side view of system (4,1), which is shown below the far-left panel in Fig. 2(a)].

According to the electronic band structure [see Fig. 3(c)], the system (4,3), is a half metal (HM) where the degeneracy

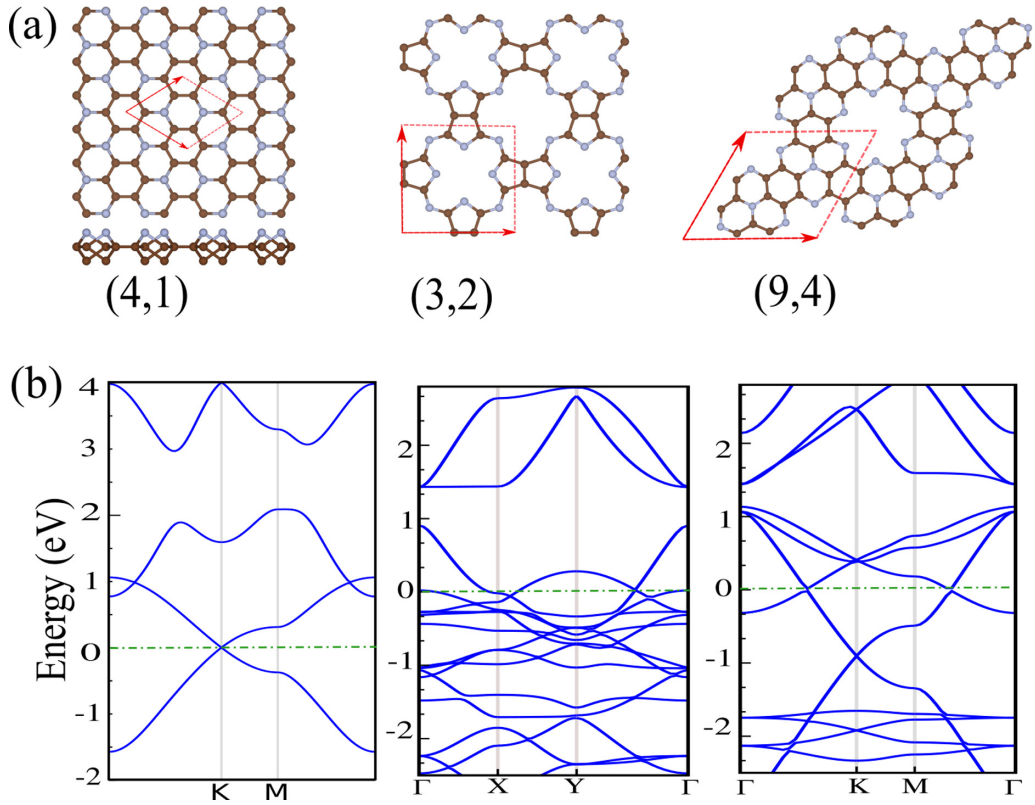

FIG. 2. (a) Geometric atomic structure of the semimetal systems (4,1) and (9,4), and metal system (3,2). (b) The corresponding electronic band structure. Here the zero of energy is set to the Fermi level. The side view of the nonplanar system (4,1) is shown below the far-left panel in (a).

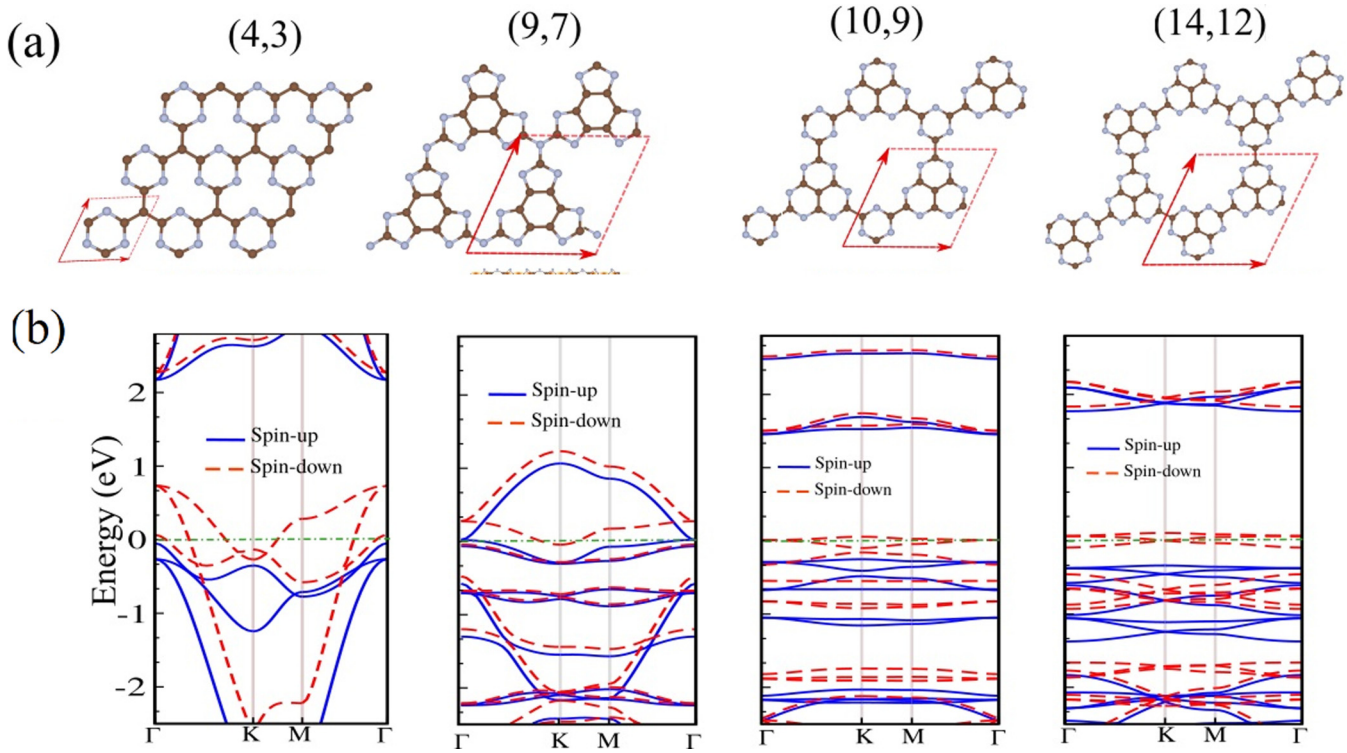

FIG. 3. (a) Geometric atomic structure of the systems (4,3), (9,7), (10,9), and (14,12). The primitive unit cell is denoted by a red parallelogram. (b) The corresponding electronic band structure. Here the zero of energy is set to the Fermi level.

of the ↑ and ↓ spin channels is broken and there is an induced $1\mu_B$ magnetic moment per unit cell. Our result is in good agreement with previous reports [20,39–41]. The valence-band maximum (VBM) and conduction-band minimum (CBM) of (4,3) originate mainly from the hybridization of the C-p_z with N-$p_{x,y}$ orbitals in the ↑ spin channel and with N-$p_{x,y}$ orbitals in the ↓ spin channel.

For the system (9,7), the energy bands cross the Fermi level (E_F), implying metallic properties [see Fig. 3(b)]. These bands are split into ↑ and ↓ spin channels, resulting in a ferromagnetic state with a magnetic moment of $0.8\mu_B$ per unit cell [37]. The electronic states near E_F arise mainly from C-p_z orbitals and from the N-p_z orbitals in the ↑ spin channel. For the systems (10,9) and (14,12), the ↓ (↑) spin channel is a gapless semimetal (semiconductor) and the VBM of the ↓ spin channel touches E_F; the spin splitting in the ↑ and ↓ spin channels induces a magnetic moment of 1 and $2\mu_B$ per unit cell, respectively. The VBM and CBM of the ↓ spin channel meet in a single point at E_F. The band gap of the systems (10,9) and (14,12) was found to be 1.7 and 2.1 eV, respectively (see Fig. 3). The latter is deduced from the ↑ spin channel, which is a feature of a spin-glass semiconductor (SG SC).

From the density of state (DOS) and partially DOS (PDOS) (we do not show them here), it can be understood that for both (10,9) and (14,12), there are sharp peaks near E_F in the ↓ spin channel, which originate from the C-$p_{x,y}$ and N-s, $p_{x,y}$ orbitals. The different spin densities of the systems (4,3), (9,7), (10,9), and (14,12), calculated from the charge density difference between the ↑ and ↓ spin channels, are shown in Fig. 3(b). The blue and yellow regions represent the ↑ and ↓ spin states, respectively. We found that the difference in spin density occurs mainly on the N atoms and the central C atoms. The contributions from the remaining C atoms are almost negligible. In addition, note that the magnetic moments are localized around the N atoms. From the shape of the isosurfaces, we found that the magnetic moments arise primarily from the sp^2-hybridized atomic orbitals on the $p_{x,y}$ instead of the p_z orbitals.

IV. STRAIN EFFECTS

Here we turn our attention to the change of bond length, lattice constant, and electronic structure as a function of tensile strain. The strain is defined as

$$\varepsilon(\%) = \frac{a - a_0}{a_0} \times 100, \tag{1}$$

where a and a_0 are strained and nonstrained lattice constants, respectively.

A. Mechanical stiffness

Before presenting the results of the effects of strain on the electronic properties of 2DGCNs, we briefly study the mechanical properties of the 2DGCNs. In order to investigate the mechanical stiffness of the studied 2DGCNs, we calculated their Young modulus by finding the variation of ground-state energy per area (E_a) of the systems with applied uniaxial strain (ε). Performing the derivation ($dE_a/d\varepsilon \simeq Y\varepsilon$) yields the stress-strain curve for the strain values up to 5% when the linear behavior is dominant. We found that for the systems with perfect hexagonal lattice, e.g., in the systems (3,1) and (4,1), the Young's modulus was found to be 1.02

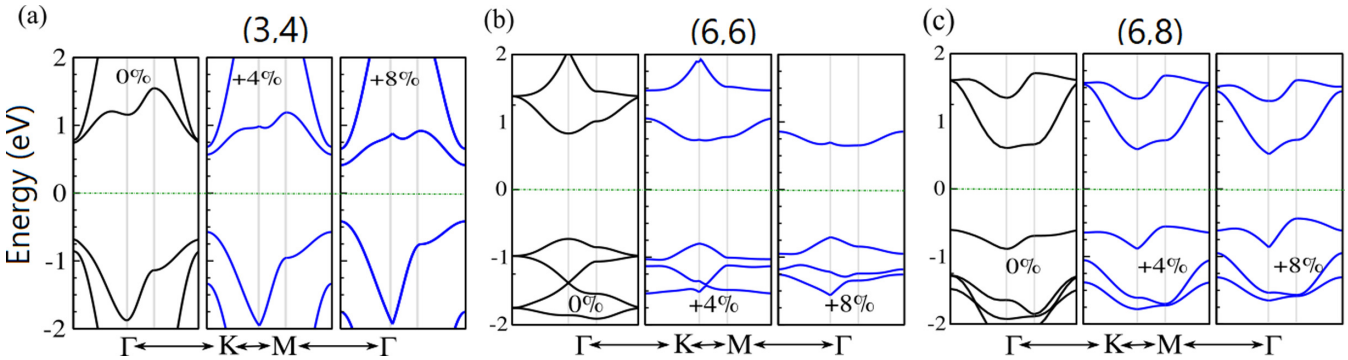

FIG. 4. The variation of the electronic band structure with applied uniaxial strain for the magnetic systems (a) (3,4), (b) (6,6), and (c) (6,8). Here the zero of energy is set to the Fermi level.

and 0.5 TPas, respectively, which is in good agreement with the results reported by Wang *et al.* [42]. For the systems with nonzero magnetic moment, we found the Young's moduli to be about 0.09, 0.03, 0.011, and 0.002 TPas, respectively. The latter results show that those systems with larger nanopore (larger D_{NP}) exhibit smaller stiffness. Notice that the breaking strain/stress is smaller for the porous systems. The Young's modulus for some of the 2DGCNs is listed in the last column of Table I. It is also interesting to note that the breaking strains for graphene and (3,1) were reported to be about 15-20%, which is equivalent to a breaking stress of about 40 N/m [42–44].

B. Nonmagnetic 2DGCN

First we study the strain effect on the electronic band structure of three semiconducting 2DGCNs. We show the electronic band structure of the systems (3,4), (6,6), and (6,8) under uniaxial strain in Fig. 4. By applying strain on the system (3,4), its band gap decreases linearly, but strain up to 2% does not change the band gap in the systems (6,6) and (6,8). The band gap in the two systems (6,6) and (6,8) only decreases linearly for $\varepsilon > 2\%$. Moreover, a large uniaxial strain applied on the system (6,6) ($\varepsilon = +8\%$) causes a direct-indirect band-gap transition. The variation of the band gap with applied strain for these systems is shown in Fig. 6(a). The best linear fit on the data of the system (3,4) is Δ (eV) $\cong -7.5\varepsilon + 1.4$. The best linear fit for the strains $\varepsilon > 2\%$ on the data of the system (6,6) is Δ (eV) $\cong -4\varepsilon + 1.2$ and on the data (6,8) is Δ (eV) $\cong -3.75\varepsilon + 1.6$.

On the other hand, before applying strain, the systems (4,1) and (9,4) are semimetal with multiple Dirac points around E_F. We found that by applying strain, their Dirac points disappear and a band gap of about a few meV is opened, i.e., a semimetal-to-semiconductor transition (see Fig. 5). There is no significant change in the band structure of the system (3,2) when subjected to strain of about +8%. The variation of the band gap with strain for the systems (4,1) and (9,4) is shown in Fig. 6(b). The best linear fit on the data of the system (9,4) is Δ (eV) $\cong 3.75\varepsilon$ and on the data of the system (4,1) is Δ (eV) $\cong 1.12\varepsilon$.

C. Magnetic 2DGCN

The investigation of the electronic properties of magnetic 2DGCN in response to the tensile strain is more interesting. The electronic band structure of the systems (4,3), (9,7), (10,9), and (14,12) under uniaxial strain in the ↑ and ↓ spin channels is shown in Figs. 7(a)–7(d). A remarkable variation in their magnetic moment happens when they are subjected to tensile strain. The latter is because of the change in the corresponding spin polarization. The system (4,3) is initially a half metal with semiconducting characteristic in the ↑ spin channel. Under uniaxial strain smaller than 4%, it remains

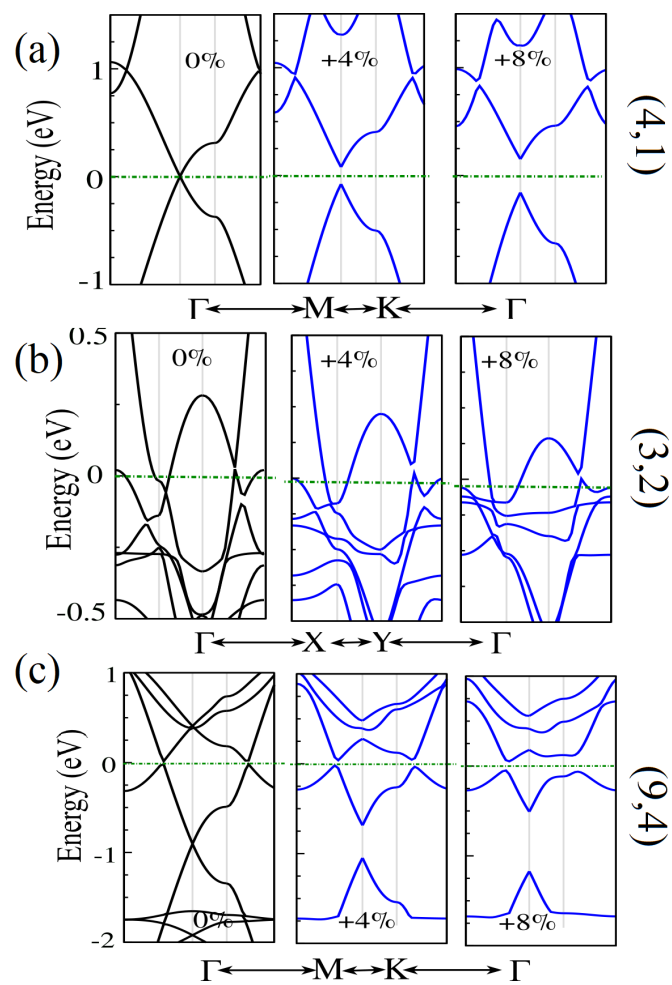

FIG. 5. The variation of the electronic band structure with applied uniaxial strain for the systems (a) (4,1), (b) (3,2), and (c) (9,4).

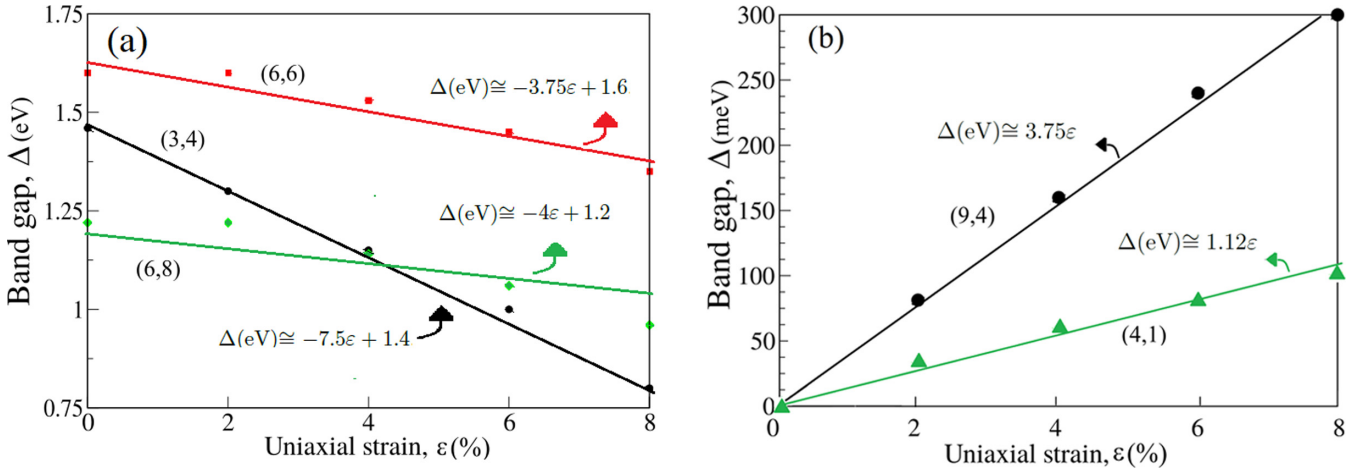

FIG. 6. The variation of the energy band gap with applied strain for (a) the systems (3,4), (6,6), and (6,8) and (b) the systems (4,1) and (9,4). The best linear fits are shown by solid lines.

half metal, but for strains larger than +8%, the VBM of the ↑ spin channel is continuously shifted upward (above the Fermi level), resulting in a ferromagnetic-metal state.

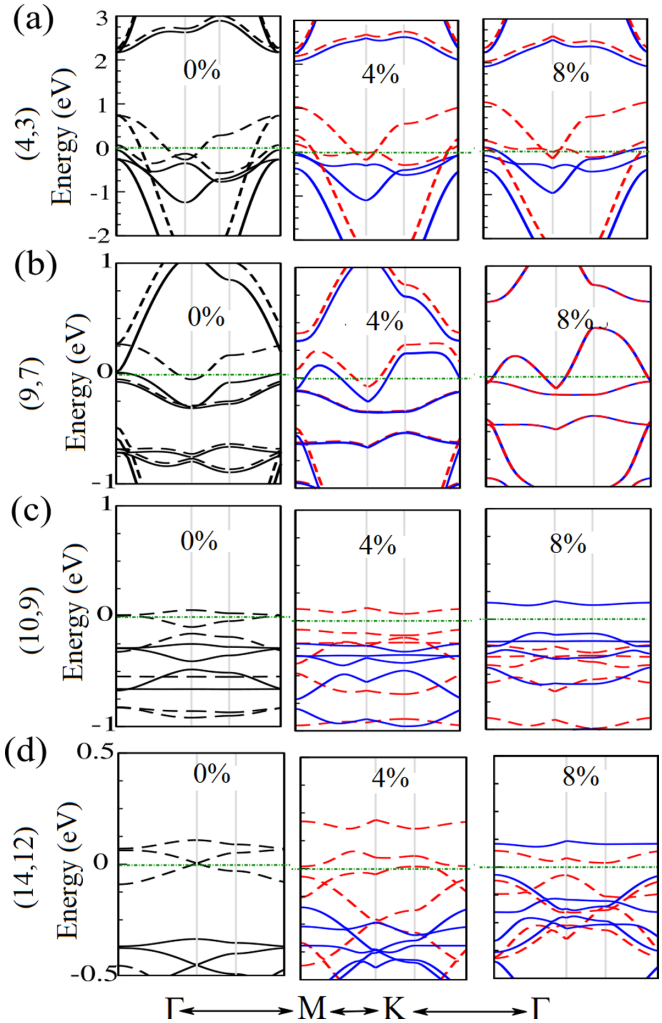

FIG. 7. Electronic band structure with applied uniaxial strain for the magnetic systems (a) (4,3), (b) (9,7), (c) (10,9), and (d) (14,12).

Interestingly, while the system (9,7) remains a ferromagnetic metal for $\varepsilon \leqslant 4\%$, when a strain larger than +6% is applied, the ferromagnetic-metal state is lost and both the ↑ and ↓ spin channels become non-spin-polarized, leading to a transition from a ferromagnetic-metal to nonmagnetic-metal state. Consequently, by increasing strain up to +6%, its magnetic moment vanishes. Also, the gapless (semimetal) state of the ↓ spin channels is eliminated in the system (10,9) under tensile strain, resulting in the opening of the band gap. Thus, the system (10,9) transforms into a dilute-semiconductor state when the strain is larger than +2%. Also, the system (14,12) for strains of 2%−4% becomes a semiconductor and, for larger strains (>8%), the system (14,12) transforms into a dilute semiconductor.

The variation of the magnetic moment of the systems (4,3), (9,7), (10,9), and (14,12) with uniaxial strain is shown in Fig. 8. The magnetic moment of the systems (4,3) and

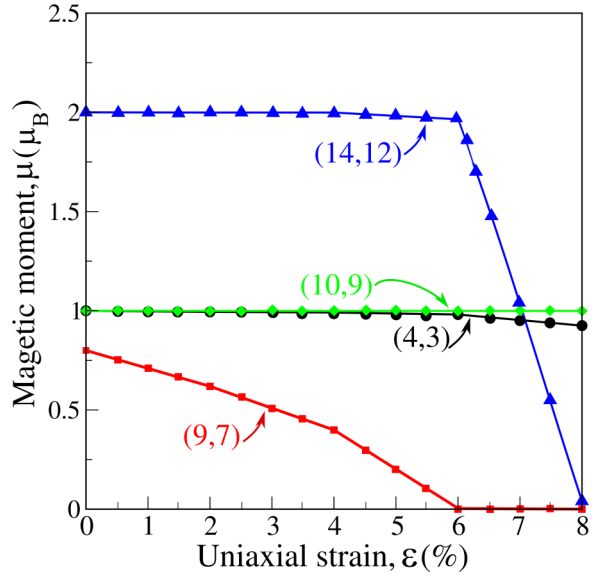

FIG. 8. The variation of the magnetic moment per unit cell of the systems (4,3), (9,7), (10,9), and (14,12) with applied strain.

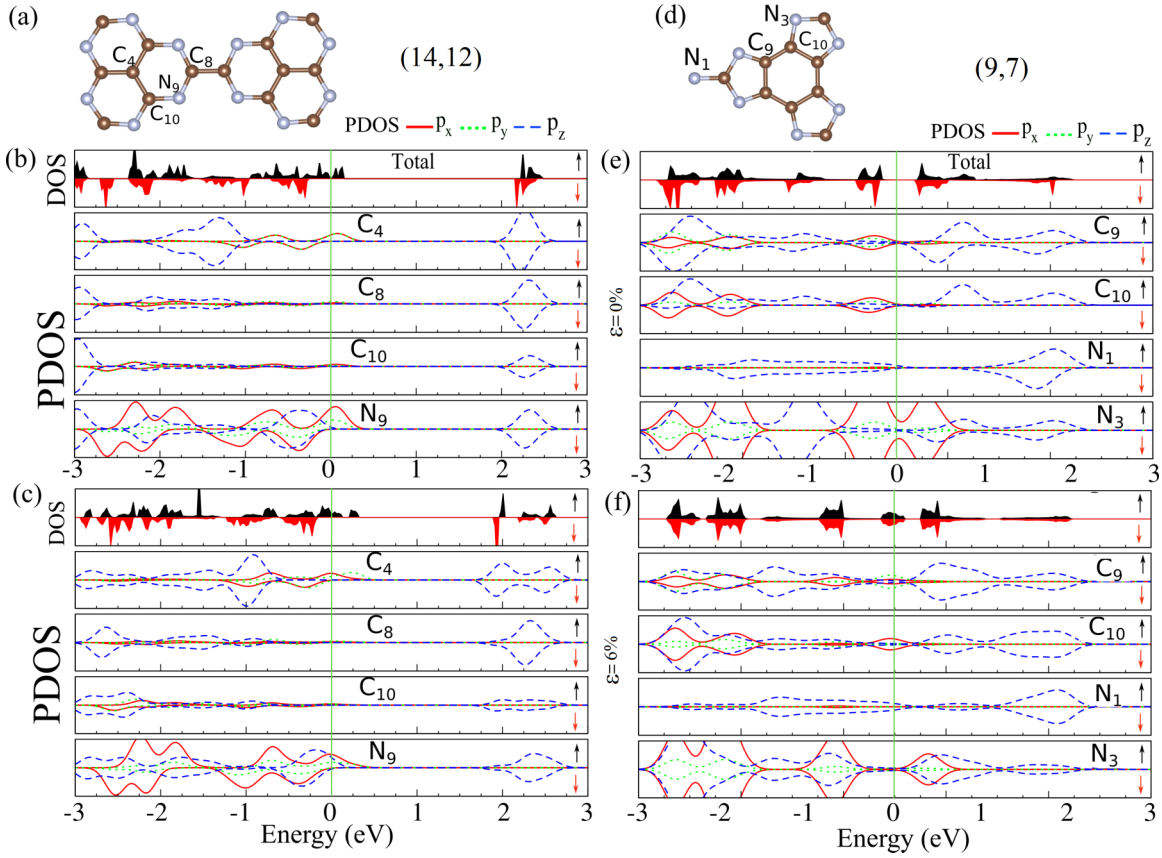

FIG. 9. The variation of the density of states (DOS) and partial density of states (PDOS) [for selected atoms, which are labeled in (a) and (d)] of two systems, (a)–(c) (14,12) and (d)–(f) (9,7), for (b),(e) 0% and (c),(f) 6% strain.

(10,9) remains approximately constant ($\sim 1\mu_B$) until reaching +8% strain. The magnetic moment decreases from $0.8\mu_B$ to zero in the system (9,7) when the strain reaches 6%. In the system (14,12), the magnetic moment sharply falls down after applying strain of +6%. Compared with the equilibrium state of the systems (4,3), (10,9), and (14,12), the splitting of the ↑ and ↓ spin channels is enhanced. It is also interesting to note that the applied uniaxial strain influences carrier mobility due to the change in the effective mass of 2DGCNs and graphene/2DGCN heterostructures [45].

To obtain further insights, we plot the variation of the density of states (DOS) and partial density of states (PDOS) of the p orbitals of the two systems (14,12) and (9,7) for two values of strain in Fig. 9. For the selected atoms [which are labeled in Figs. 9(a) and 9(d)], the corresponding DOS and PDOS are shown in Fig. 9. Once these systems are in the relaxed state ($\varepsilon = 0\%$), the spin-up and spin-down PDOS are clearly different. However, by applying a strain of about 6% on the system (9,7), the ferromagnetic state disappears. The spin-up and spin-down PDOS of the N atoms in the system (9,7) become symmetric under a strain of 6%, while the PDOS of the N atom in the system (14,12) keeps its asymmetrical properties, and hence the ferromagnetic ordering is still stable; see Fig. 9(c). It is seen that the stable ferromagnetic ordered state in (14,12) is related to the asymmetry in the p_x (or p_y) orbital rather than p_z orbital [see the red curve for the PDOS calculated on the N_9 atom in Fig. 9(c)]. The stable ferromagnetic ordering state can be explained using a tight-binding (TB) model with strong spin-orbit interaction [1]. In fact, in TB calculations, four distance-dependent nearest-neighbor hopping parameters and an exchange field parameter are involved. The band structure of the TB model is found to be in good agreement with the spin-polarized bands given by the DFT calculations [1].

V. CONCLUSION

In summary, we presented extensive first-principles calculations to investigate the structural, electronic, and magnetic properties of 12 two-dimensional graphitic carbon nitrides. We showed that the systems (4,1) and (9,4) are semimetal with one and multiple Dirac points around the Fermi level, while the (3,2) is a metal. The systems (2,1), (3,1), (3,4), (6,6), and (6,8), exhibit semiconducting features with 1.75, 0.4, 1.45, 1.5, and 1.22 eV band gaps, respectively. Among the studied systems, the systems (4,3), (9,7), (10,9), and (14,12) exhibit magnetic features (although there is no metallic element in the system) with magnetic moments in the range $\sim 0.8-2\mu_B$. We found that while the system (4,3) is a half metal, the system (9,7) is a ferromagnetic metal. In particular, we showed that the band structure of 2DGCN nanosheets can be adjustable by applying strain. Depending on the (n, m) values, various behavior in the electronic structure of the systems can be found. For instance, the ferromagnetic ordered state in the systems

(4,3), (10,9), and (14,12) remains stable in the presence of a strain of about 6%. However, the system (9,7) loses its ferromagnetic ordering by increasing the strain. This is due to the presence of topological defects in the (9,7) system, which reduces the asymmetry between the spin up and spin down of the p_z orbitals in the considered range of strain. Moreover, applying strain causes a remarkable gap opening in the systems which are initially semimetal. Also, the gap is closed linearly by applying strain in those systems which are initially a semiconductor.

[1] X. Zhang and M. Zhao, RSC Adv. **5**, 9875 (2015).
[2] M. Javeed, K. L. Eun, J. Minbok, S. Dongbin, J. In-Yup, J. Sun-Min, C. Hyun-Jung, S. Jeong-Min, B. Seo-Yoon, S. So-Dam, P. Noejung, H. O. Joon, S. Hyung-Joon, and B. Jong-Beom, Nat. Commun. **6**, 6486 (2015).
[3] M. Javeed, E. K. Lee, M. Jung, D. Shin, H-J. Choi, J.-M. Seo, S-M. Jung, D. Kim, F. Li, M. S. Lah, N. Park, H.-J. Shin, J. H. Oh, and J.-B. Baek, Proc. Natl. Acad. Sci. **113**, 7414 (2016).
[4] A. Bafekry and M. Neek-Amal, Phys. Rev. B **101**, 085417 (2020).
[5] H. Ghorbanfekr-Kalashami, M. Neek-Amal, and F. M. Peeters, Phys. Rev. B **93**, 174112 (2016).
[6] E. Lotfi and M. Neek-Amal, J. Mol. Graphics Modell. **74**, 100 (2017).
[7] J. Beheshtian, A. Sadeghi, M. Neek-Amal, K. H. Michel, and F. M. Peeters, Phys. Rev. B **86**, 195433 (2012).
[8] Q. Zhou, M. Wu, M. Zhang, G. Xu, B. Yao, C. Li, and G. Shi, Mater. Today Energy **6**, 181 (2017).
[9] S. U. Lee, R. V. Belosludov, H. Mizuseki, and Y. Kawazoe, Small **5**, 1769 (2008).
[10] J. Li, W. Cui, Y. Sun, Y. Chu, W. Cen, and F. Dong, J. Mater. Chem. A **5**, 9358 (2017)
[11] Y. Zheng, J. Liu, J. Liang, M. Jaroniec, and S. Zh. Qiao, Energy Environ. Sci. **5**, 6717 (2012).
[12] B. Mortazavi, O. Rahaman, T. Rabczuk, and L. F. C. Pereira, Carbon **106**, 1 (2016).
[13] A. Bafekry, S. F. Shayesteh, and F. M. Peeters, J. Phys. Chem. C. **123**, 12485 (2019).
[14] M. Makaremi, B. Mortazavi, and C. V. Singh, Phys. Chem. C **121**, 18575 (2017).
[15] A. Bafekry, C. Stampfl, S. F. Shayesteh, and F. M. Peeters, Adv. Elec. Mater. **5**, 1900459 (2019).
[16] B. Mortazavi, Carbon **118**, 25 (2017).
[17] A. Bafekry, M. Ghergherehchi, S. Farjami Shayesteh, and F. M. Peeters, Chem. Phys. **526**, 110442 (2019).
[18] M. B. Tagani and S. I. Vishkayi, J. Appl. Phys. **124**, 084304 (2018).
[19] A. Bafekry, S. F. Shayesteh, and F. M. Peeters, Phys. Chem. Chem. Phys. **21**, 21070 (2019).
[20] A. Du, S. Sanvito, and S. C. Smith, Phys. Rev. Lett. **108**, 197207 (2012).
[21] A. Wang, X. Zhang, and M. Zhao, Nanoscale **6**, 11157 (2014).
[22] A. Thomas, A. Fischer, F. Goettmann, M. Antonietti, J.-O. Maller, R. Schlagl, and J. M. Carlsson, J. Mater. Chem. **18**, 4893 (2008).
[23] G. Algara-Siller, N. Severin, S. Y. Chong, T. Bjarkman, R. G. Palgrave, A. Laybourn, M. Antonietti, Y. Z. Khimyak, A. V. Krasheninnikov, J. P. Rabe, U. Kaiser, A. I. Cooper, A. Thomas, and M. J. Bojdys, J. Angew. Chem. **126**, 7580 (2014).
[24] X. Li, J. Zhou, Q. Wang, Y. Kawazoe, and P. Jena, J. Phys. Chem. Lett. **4**, 259 (2013).
[25] J. P. Perdew, K. Burke, and M. Ernzerhof, Phys. Rev. Lett. **77**, 3865 (1996).
[26] T. Ozaki, Phys. Rev. B **67**, 155108 (2003).
[27] N. Troullier and J. L. Martins, Phys. Rev. B **43**, 1993 (1991).
[28] T. Ozaki and H. Kino, Phys. Rev. B **69**, 195113 (2004).
[29] H. J. Monkhorst and J. D. Pack, Phys. Rev. B **13**, 5188 (1976).
[30] L. Zhu, Q. Xue, X. Li, T. Wu, Y. Jin, and W. Xing, J. Mater. Chem. A **3**, 21351 (2015).
[31] Y. Yuanyuan, F. Li, H. Zhou, and M. Zhao, Sci. Rep. **6**, 19952 (2016).
[32] B. Xu, H. Xiang, Q. Wei, J. Q. Liu, Y. D. Xia, J. Yin, and Z. G. Liu, Phys. Chem. Chem. Phys. **17**, 15115 (2015).
[33] S. Mizuno, F. Mitsutaka, and K. Nakao, Synthetic Metals **71**, 1869 (1995).
[34] X. Li, Y. Dai, Y. Ma, S. Han, and B. Huang, Phys. Chem. Chem. Phys. **16**, 4230 (2014).
[35] H. Chen, S. Zhang, W. Jiang, C. Zhang, H. Guo, Z. Liu, Z. Wang, F. Liu, and X. Niu, J. Mater. Chem. A **6**, 11252 (2018).
[36] E. Kroke, M. Schwarz, E. Horath-Bordon, P. Kroll, B. Noll, and A. D. Norman, New J. Chem. **26**, 508 (2002).
[37] H. Li, H. Hu, C. Bao, J. Hua, H. Zhou, X. Liu, X. Liu, and M. Zhao, Phys. Chem. Chem. Phys. **17**, 6028 (2015).
[38] X. Zhang, A. Wang, and M. Zhao, Carbon **84**, 1 (2015).
[39] T. Hu, A. Hashmi, and J. Hong, Sci. Rep. **4**, 6059 (2014).
[40] A. Hashmi and J. Hong, Sci. Rep. **4**, 4374 (2014).
[41] H. Wu, Y. Liu, E. Kan, Y. Ma, W. Xu, J. Li, M. Yan, R. Lu, J. Wei, and Y. Qian, Appl. Phys. **49**, 295301 (2016).
[42] H. Wang, H. Wu, and J. Yang, arXiv:1703.08754.
[43] E. Cadelano, P. L. Palla, S. Giordano, and L. Colombo, Phys. Rev. Lett. **102**, 235502 (2009).
[44] C. Lee, X. Wei, J. W. Kysar, and J. Hone, Science **321**, 385 (2008).
[45] M. M. Dong, C. He, and W. X. Zhang, J. Mater. Chem. C **5**, 3830 (2017).